Journal of Magnetism and Magnetic Materials 655 (2026) 174253

Contents lists available at ScienceDirect

Journal of Magnetism and Magnetic Materials

journal homepage: www.elsevier.com/locate/jmmm

The impact of rare earth ions on the magnetic properties of $Li_{0.4}Zn_{0.4}Fe_{2.2}O_4$ spinel ferrites in contradiction to prior studies

Ebtesam E. Ateia [a,*], Omnia younes [a], M.M. Arman [a], Y.A. Saeid [a,b]

[a] Physics Department, Faculty of Science, Cairo University, Giza, Egypt
[b] Higher Institute of Engineering and Technology, Fifth Settlement, Cairo, Egypt

ARTICLE INFO

Keywords:
Magnetic moment
Rare earth
Spinel ferrite
Waste-water
Switching field distribution

ABSTRACT

The novelty of the present work lies in the preparation of non-stoichiometric $Li_{0.4}Zn_{0.4}Sm_{0.025}Fe_{2.2}O_4$ and $Li_{0.4}Zn_{0.4}Nd_{0.025}Fe_{2.2}O_4$ with the same metal ratio as part of $Li_{0.4}Zn_{0.}$ $Fe_{2.2}O_4$, but with an excess of rare earth ions (RE^{3+}). The samples were synthesized using the citrate auto-combustion method, and various characterization techniques were utilized for their analysis. The X-ray diffraction (XRD) spectra indicate the presence of a crystalline phase. The average crystallite size is observed to range from 15 to 19 nm. Rietveld refinement is conducted utilizing the FullProf software for pattern-fitting structure refinement, to accurately determine the structural parameters. A vibrating sample magnetometer (VSM) was utilized to evaluate the magnetic parameters, revealing that the incorporation of Nd^{3+} and Sm^{3+} ions led to an improvement in the saturation magnetization. The bond length (BL) and bond angles (θ) between cations (Me–Me) and cation–anion (Me–O) have been estimated. The reduction in θ3 and θ4 implies a weakening of B–B interactions, while the increase in θ1, θ2, and θ5 among several factors indicates a strengthening of the AB interaction. The fluctuations in the Fe^{2+} (4 μB) /Fe^{3+} (5 μB) ratio can greatly alter the magnetic moment by affecting electron configuration and exchange interactions. A decrease in spin canting, particularly at surfaces or grain boundaries, also plays a role by enhancing spin alignment and boosting the effective magnetization. The ad-sorption behavior can be characterized by the Langmuir, and Freundlich isotherm models. The maximum ad-sorption capacities have been found to be 90% for Pb^{2+} ions. It is concluded that the pseudo-second order model is more appropriate for describing the ad-sorption kinetic data compared to the pseudo-first order model and inter-particle diffusion model.

1. Introduction

Ferrites are magnetic iron oxide compounds that can be categorized into spinel ferrite (SFs), hexaferrite, garnet, and orthoferrites. SFs have the formula MFe_2O_4, where M represents a divalent cation and Fe is typically in the trivalent state [1,2]. The arrangement of divalent and trivalent ions within the unit cell determines the type of SFs, which can be classified as normal, inverse or mixed [3]. SFs offer several key advantages [4,5], including a high specific surface area, thermal and chemical stability, excellent magnetic properties, tunable size and shape, low cost, good catalytic activity, and mechanical hardness.

Several methods are employed in the synthesis of SFs such as co-precipitation [6,7]. hydrothermal [8,9], sol-gel [10,11], sono chemical [12,13], and microemulsion [14] methods.

The citrate combustion technique, is chosen for the synthesis of the samples in the present study, due to its ease of implementation [15], and production of excellent phase purity [1,16].

In addition to its low cost, time efficiency, and capability of producing uniform and nano sized ferrite particles, making it suitable for large-scale production of nanoparticles (NPs) with a high surface area. The group of rare-earth (RE) elements comprises 17 constituents. When a RE ion is incorporated into SFs, the spin coupling effect and the $3d^5$–$4f^7$ coupling effect impact the characteristics of the ferrite [17]. The properties of SFs are greatly affected by the larger RE radii [18].

For doping applications, a significant challenge associated with a SFs structure lies in selecting an appropriate element that is compatible with Fe^{3+} cations at the B site. Consequently, a lower concentration of RE cations is the optimal choice for B-site doping due to their compatibility with Fe^{3+} cations [19].

The incorporation of RE elements such as neodymium (Nd^{3+}) and samarium (Sm^{3+}) into SFs often leads to modifications in the crystal lattice of SFs, enhancing the stability of the material under diverse

* Corresponding author.
E-mail address: ebtesam@sci.cu.edu.eg (E.E. Ateia).

https://doi.org/10.1016/j.jmmm.2026.174253
Received 15 November 2025; Received in revised form 6 May 2026; Accepted 19 May 2026
Available online 27 May 2026

environmental conditions. This stability is crucial for the reproducibility and reliability of electronic materials, ensuring optimal performance throughout their lifecycle [20]. Both Nd and Sm possess strong magnetic moments, which can improve the overall magnetic performance of the SFs [21]. This can result in higher saturation magnetization (Ms) and better magnetic stability. Furthermore, they lead to higher coercivity in ferrite materials, making them more resistant to demagnetization and suitable for high-performance applications like permanent magnets [22].

The unique properties imparted by RE doping can enable the use of SFs in a broader range of applications, including magnetic devices such as permanent magnets, loudspeakers, electric motors, and transformers. In nanomedicine, SFs are utilized in drug delivery systems, as biological tissues are transparent to magnetic fields [23].

Li-ferrites are characterized by their low cost, excellent ferrimagnetic properties, high Curie temperature, and minimal microwave dielectric loss [24]. The small amount of doping in Li-ferrites by RE ions or transition metals (TMs) enhances their physical properties and applications [25,26]. On the other hand, due to the high surface area of zinc SFs, they are employed in waste treatment and in sensors for detecting toxic gas emissions from industrial processes [27],

Industries such as mining, paints, coatings, fertilizers, metal plating, batteries and electronic waste are major sources that discharge heavy metals (HMs) into the environment, either directly or indirectly. The United States Environmental Protection Agency (US EPA) has established maximum contaminant level (MCLs) for various HMs in water, beyond which they are considered toxic to human health. For Chromium, Lead and Cadmium the MCLs are 0.05, 0.006 and 0.01 mg/L, respectively [28]. The goal of this work is to remove HMs from water. The ad-sorption process can occur through physical or chemical mechanisms. Physical interactions involve weak intermolecular forces, while chemical interactions involve the formation of strong bonds between the ad-sorbate and the ad-sorbent. Many factors influencing ad-sorption efficiency include the surface properties of the ad-sorbent, the concentration of the ad-sorbate, pH and temperature [29]. In recent years, researchers have increasingly adopted the use of RE cations as doping ions in SFs, with the objective of altering their structural, magnetic, and other diverse properties. Furthermore, magnetic SFs have become widely employed for the elimination of toxic contaminants from water [23].

In the present study, $Li_{0.4}Zn_{0.4}RE_xFe_{2.2}O_4$ (where x = 0 and 0.025; RE denotes RE ions, specifically Nd^{3+} and Sm^{3+}) was synthesized using the citric combustion technique. The innovation of this synthesis is characterized by the incorporation of Nd^{3+} and Sm^{3+} ions as extra dopants while maintaining the metal ratio of the parent sample $Li_{0.4}Zn_{0.4}Fe_{2.2}O_4$. The structural and functional properties of the synthesized NPs were investigated through various techniques. The impact of the RE ions on the physical properties of $Li_{0.4}Zn_{0.4}Fe_{2.2}O_4$ was evaluated, with a particular focus on the $Li_{0.4}Zn_{0.4}Sm_{0.025}Fe_{2.2}O_4$ NPs. It was specifically examined for its potential use as heavy metal ad-sorbents in water treatment applications.

2. Experimental work

2.1. Materials

The metal nitrates ($LiNO_3.3H_2O$, $Zn(NO_3)_2.6H_2O$, $Fe(NO_3)_2.9H_2O$, $NdCl_3.6H_2O$, and $SmCl_3.6H_2O$) were purchased from Sigma Aldrich company with a purity of 99.99%.

2.2. The preparation of $Li_{0.4}Zn_{0.4}RE_{0.025}Fe_{2.2}O_4$ (LZFRO) NPs

$Li_{0.4}Zn_{0.4}RE_xFe_{2.2}O_4$ was synthesized using the citric combustion method [30] as illustrated in Fig. 1. The stoichiometric ratio of metal nitrates and citric acid was dissolved in 20 ml of deionized water, with the metal nitrate to citric acid ratio maintained at 1:1. The solution was heated and stirred on a magnetic stirrer at 80° for one hour after adjusting the pH to 7 using ammonia solution. After the solution reached homogeneity, the samples were heated at 200 °C to evaporate all distilled water and form the ash. The resulting brown brittle ash was ground and sintered at 600 °C with a heating rate of 4 °C/min [31,32].

2.3. Removal of heavy metals (RHMs)

To investigate the effectiveness of $Li_{0.4}Zn_{0.4}Sm_{0.025}Fe_{2.2}O_4$ in removing HM ions, experiments were conducted where 0.007 g of lead was added to 100 ml of deionized water and then 0.1 g of LZFSO ad-sorbent was dissolved in the simulated waste-water. The solutions were thoroughly mixed using an electric shaker at 200 rpm for 105 min. The effect of contact time, optimum pH values and ad-sorption techniques for the removal of HM (Pb^{2+}) ions were investigated. To calculate the quantities of metal ions ad-sorbed per unit mass of the ad-sorbent during time t (q_t) and the removal efficiencies (η) the following equations were used [33]:

$$q_{t=V(C_0-C_t)/m} \quad (1)$$

$$\text{Removal efficiency\%}\eta = (C_0 - C_t/C_0)*100 \quad (2)$$

Where C_0 is the initial concentration of lead ions at zero time, C_t is the concentration of lead ions at time t (mg/l), *V* denotes the volume (L) of the aqueous solution and m is the mass of ad-sorbent used (g). The concentration of Pb^{2+} ions was determined using atomic absorption spectrophotometry (ICP spectrometry Prodigy 7). The ad-sorption efficiency % and the time dependent ad-sorption capacity (q_t) of metal ions

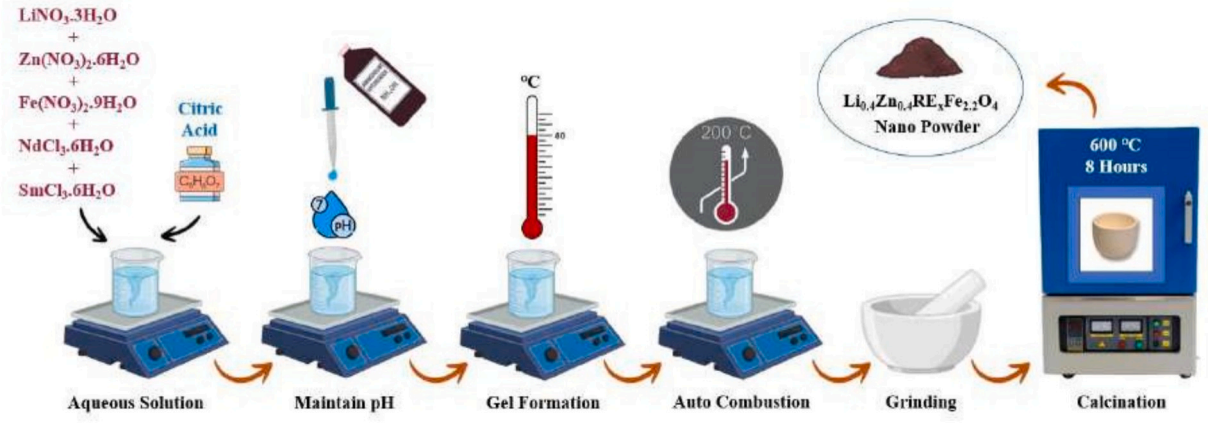

Fig. 1. The diagram illustrating the citrate auto-combustion process.

were estimated for the samples in the forthcoming data.

2.4. Characterizations

The crystal structure of the investigated samples was analyzed using an X-ray diffractometer (Proker D8 advanced, XRD), and the obtained data were indexed with ICDD card number 02–022-0066. Surface morphology and nanostructures were studied using Field Emission Scanning Electron Microscopy (FESEM) with a Quanta 250 FEG SEM system which includes an energy-dispersive X-ray spectroscopy (EDX) unit made by FEI company (USA). Raman spectroscopy (RS) was conducted at room temperature (25 °C) in the wavenumber range of 100–1800 cm^{-1} using a Horiba Lab Ram HR Evolution spectrometer (Horiba Ltd., UK). Porosity and surface area were assessed using the Brunauer-Emmett-Teller (BET) method (NLDFT Ads. model). The effect of the magnetic field on the magnetization was investigated using a vibrating sample magnetometer (VSM, Lakeshore 7410S).

3. Results and discussion

3.1. Structural analyses

3.1.1. X-ray analysis (XRD)

The incorporation of Nd^{3+}/Sm^{3+} ions as excess cations in SFs often leads to the formation of a non-stoichiometric structure, since these trivalent cations exceed the normal cation balance of the ideal AB_2O_4lattice. Consequently, excess RE^{3+} incorporation induces cation redistribution, modifying the inversion degree of the spinel structure [34]. In order to maintain overall charge neutrality, the lattice compensates through several mechanisms, including the formation of oxygen vacancies, partial reduction of Fe^{3+} to Fe^{2+}, or the generation of cation vacancies.

Fig. 2a–c illustrates the X-ray diffraction (XRD) pattern of the synthesized $Li_{0.4}Zn_{0.4}Fe_{2.2}O_4$ (LZFO), $Li_{0.4}Zn_{0.4}Nd_{0.025}Fe_{2.2}O_4$ (LZFNO) and $Li_{0.4}Zn_{0.4}Sm_{0.025}Fe_{2.2}O_4$ (LZFSO). The XRD data are analyzed and compared with the standard reference pattern (ICDD) Card No. 02–022-0066, confirming the formation of a single-phase cubic spinel structure. The most intense diffraction peak is indexed at 2θ equals 35.8°, corresponding to the (311) crystallographic plane, which is characteristic of SFs.

The figure demonstrates the changes in the position and broadening of the primary diffraction planes resulting from the addition of RE^{3+} ions into the LZFO structure. These changes are attributed to the integration of Nd^{3+} (0.983 Å) and Sm^{3+} (0.958 Å), which possess large ionic radii, into the LZFO samples. This incorporation induces a stress field within the LZFO crystal lattice, leading to shifts of the main crystallographic planes towards the high-angle region, which in turn causes a reduction in the interplanar distance and consequently a decrease in D [28].

Rietveld refinement is carried out to further validate the crystal structure of the stoichiometric and non-stoichiometric prepared samples, and the corresponding data are presented in Fig.2a–c and Table 1. Rietveld refinement is conducted utilizing the FULLPROOF software for pattern-fitting structure refinement, to accurately determine the structural parameters. During the refinements, XRD patterns are computed assuming a cubic Fd-3 m spinel structure, which includes Wyckoff sites 8a and 16d for atoms in the tetrahedral A- and octahedral B-sites. It is widely recognized that Zn^{2+} prefers A sites, while Li^{1+} and RE^{3+} ions tend to favor B sites, due to significant stabilization energy within the structures. Conversely, Fe is distributed between both A and B sites.

The agreement factors presented in Table 1 reflect a moderate level of refinement quality. Furthermore, the goodness-of-fit value (χ^2) lies within an acceptable range (typically 1–3), indicating that the statistical agreement between experimental and simulated data, is reasonable.

The incorporation of RE^{3+} ions as excess dopants into spinel ferrites produces a noticeable variation in the oxygen positional parameter u(where $x = y = z = U$) obtained from Rietveld refinement, (Table 1)

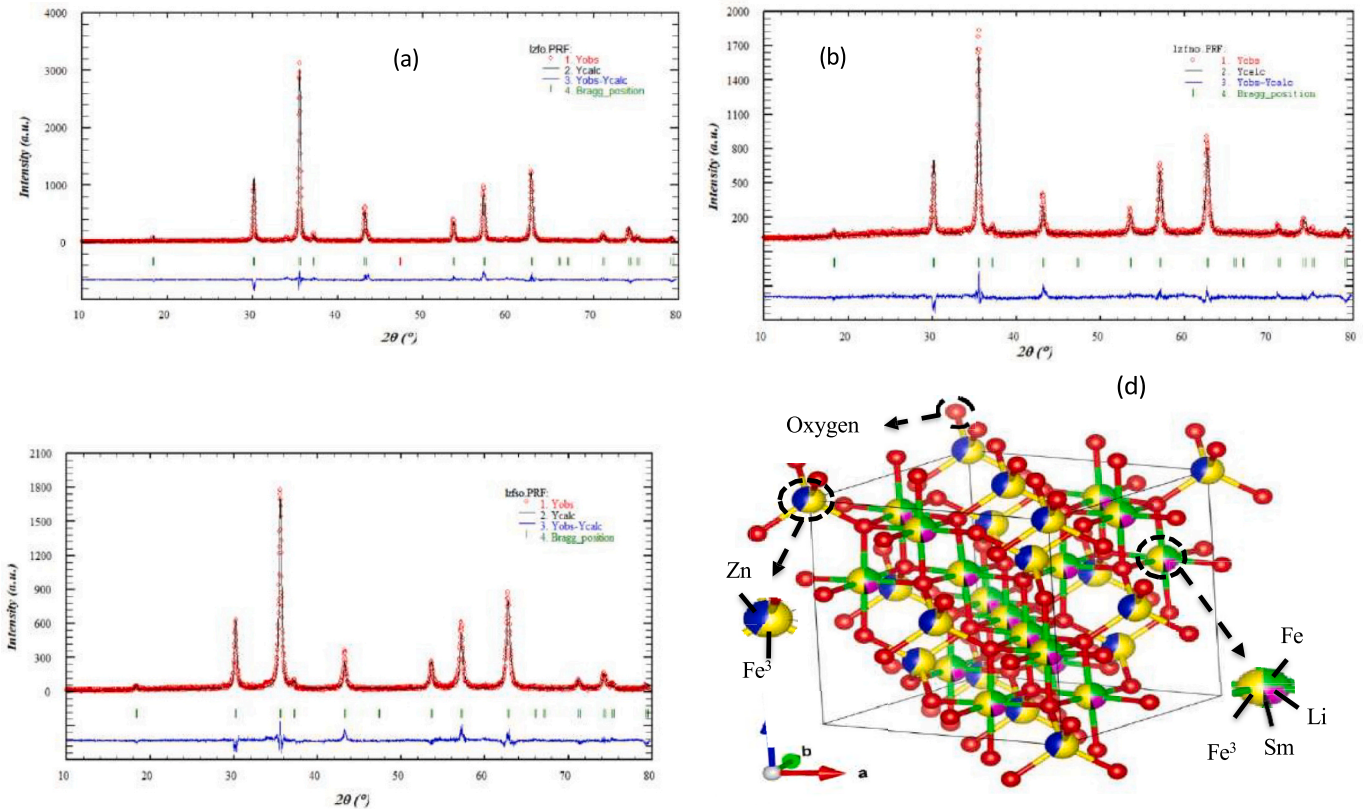

Fig. 2. a–c XRD pattern of LZFO, LZFNO and LZFSO with the refinement chart and (d) Schematic representation of cation distribution in the sample.

Table 1
The cation distributions, the crystallite size (D), theoretical and experimental lattice parameters (a), theoretical density (Dx), Rietveld Refinement parameters, radii of A and B sites, dislocation density (ρ), and bond distances.

The Cation distribution	D(nm)	a_{exp} (Å)	a_{theo} (Å)	D_x gm/cm^3	X = y = z = *U*	R_{exp} %	χ^2	r_A (Å)	r_B (Å)	$\rho(10^{-3} \times nm^{-2})$	Bond Distances A – O	Bond Distances B – O
$(Zn^{2+}_{0.4}Fe^{3+}_{0.6})_{IV}$ $\lvert Li^{1+}_{0.4}\ Fe^{2+}_{0.7}\ Fe^{3+}_{0.9}\rvert_{VI}$	19.190	8.281	8.282	5.050	0.254	16.790	2.06	0.534	0.715	2.720	1.854	0.250
$(Zn^{2+}_{0.4}\ Fe^{3+}_{0.6})_{IV}\ \lvert Li^{1+}_{0.4}\ Fe^{2+}_{0.64}Fe^{3+}_{0.96}\ Nd^{3+}_{0.025}\rvert_{VI}$	16.990	8.303	8.304	5.090	0.275	19.490	2.21	0.534	0.723	3.460	1.854	0.252
$(Zn^{2+}_{0.4}\ Fe^{3+}_{0.6})_{IV}\ \lvert Li^{1+}_{0.4}\ Fe^{2+}_{0.53}Fe^{3+}_{1.07}\ Sm^{3+}_{0.025}\rvert_{VI}$	15.330	8.283	8.283	5.130	0.265	17.440	2.16	0.534	0.716	4.260	1.854	0.250

reflecting structural adjustments within the lattice. Due to their significantly larger ionic radii compared to Fe^{3+}, Nd^{3+}/Sm^{3+} ions tend to occupy B sites generating lattice strain and local distortion. This size mismatch forces the surrounding oxygen ions to shift from their ideal positions in order to maintain structural stability, which is directly captured by changes in the refined *U* parameter.

Furthermore, the variation of *U* with excess RE^{3+} (0.025) incorporation reflects not only lattice expansion but also the imbalance between A- and B-site ionic radii and the redistribution of cations within the spinel structure. As reported, the U serves as a sensitive indicator distinguishing the relative expansion of the two sublattices and the degree of structural distortion induced by incorporation. Therefore, the evolution of *U* with Nd^{3+}/Sm^{3+} excess provides direct evidence of oxygen sublattice displacement, cation redistribution, local distortion, modified bond geometry, and the creation of vacancies.

The Oxygen position parameter (*u*) is determined as mentioned in the previous work [35] with an approximate value of 0.379 Å for the prepared samples. A small deviation from the u" parameter for the ideal spinel which has a value nearly equal to 0.375 is detected. In the actual spinel lattice u is greater than 0.375. This deviation is due to the shifting of the origin at the B sites as the number of cation ions increases (>2).

The "D" of the synthesized samples is estimated using the Scherer equation [36], and tabulated in the Table

$$D = 0.9\lambda/\beta\cos\theta \tag{3}$$

where λ is the X-ray wavelength (1.5406 Å), β is the full width at half maximum (FWHM) of the diffraction peak, and θ is the Bragg diffraction angle. [37]. Notably, upon the incorporation of Nd^{3+}/ Sm^{3+} a systematic shift to higher 2θ suggests a reduction in size (D). This modification pertains to the change in the nucleation and growth rates of the samples that have been prepared.

Additionally, the experimental lattice parameter (a) is calculated using the following equation and is presented in the Table [38].

$$\frac{1}{d^2} = h^2 + k^2 + l^2 \Big/ a^2 \tag{4}$$

where *d* represents the interplanar spacing, while h, k, and l are the Miller indices.

B. Venkatesh et al. [39] investigated that, doped samples with larger ionic radii of Ho^{3+} (0.90 Å) and Ce^{3+}(1.14 Å) ions prevent their ability to occupy A and B sites but form aggregates at the grain boundary; consequently, the lattice constantly decreases with the doping of RE ions. In contrast to Venkatesh, the present study reveals that the incorporation and not the doping of RE ions with large ionic radii, such as Nd^{3+} ($r_{Nd^{3+}} = 0.983$ Å) or Sm^{3+} ($r_{Sm^{3+}} = 0.958$ Å), into the LZFO structure results in their preferential occupation of the B-site. This addition causes an expansion of the lattice, which in turn increases the lattice parameter (a) and impacts their physical properties as will be mentioned later.

The theoretical density (D_x) [40] of the sample is calculated using Eq. (5)

$$D_x = 8M/N_A V \tag{5}$$

where *M* is the molecular weight of the sample, N_A is Avogadro's number, *V* is the unit cell volume, and the factor 8 represents the number of formula units per unit cell [41].

The D_x of the LZFO sample increases upon incorporation with Sm^{3+} or Nd^{3+} ions due to the difference in molecular masses between Sm^{3+} / Nd^{3+} and Fe^{3+} ions. The incorporation of Sm^{3+} or Nd^{3+} at the B-site alters the overall molecular weight, leading to an increase in (D_x), as reported in the Table.

Dislocation density (**ρ**) is calculated using the following Eq. [42].

$$\rho = 1/D^2 \tag{6}$$

The calculated values of ρ are reported in Table 1. The ρ increases with the incorporation of Nd^{3+} and Sm^{3+} due to the induced lattice strain (ε), which increases the internal stress on the crystal structure.

The theoretical lattice parameter (a_{th}) is determined in the following manner [43].

$$a_{th} = 8\Big/3\sqrt{3}\left[(r_A + R_\circ) + \sqrt{3}\,(r_B + R_\circ)\right] \tag{7}$$

where $R_\circ$ is the radius of the oxygen ion, which is taken as 1.32 Å, while the radii of A-site (r_A), and B-site (r_B) are calculated using following equations [44].

$$r_A = \sum \delta\, r_{cation}\ r_B = 1\Big/2\sum \delta\, r_{cation} \tag{8}$$

where δ represents the ratio of cations occupying the A and B sites. The calculated values of a_{th} are compared with the experimental lattice constants and the suggested distribution of the samples is depicted in Table1.

The bond distances between metal cations and oxygen ions at the tetrahedral (A—O) and octahedral (B—O) sites are given by the following Eqs. [45].

$$A - O = a\sqrt{3}(u - 1/4), B - O = a\left(3u^2 - 11u/4 + 43/64\right)^{1/2} \tag{9}$$

The computed bond distances (BD) are represented in the Table. It is evident that the BD of the A sites remain unchanged. This change affect A—B and B—B interaction, as will be discussed later.

3.1.2. FESEM

FESEM provides high-resolution images that reveal the uniformity, agglomeration behavior, and grain boundary characteristics of the prepared NPs (Fig. 3**)**. The micrographs reveal that the NPs exhibit significant agglomeration, primarily due to their strong magnetic interactions. This behavior is common in magnetic NPs, where dipole-dipole interactions lead to the formation of clusters, reducing their overall free energy.

Among the samples, LZFSO shows the highest degree of agglomeration, which correlates with its higher magnetization, limiting their dispersion. This effect can influence the material's surface area, porosity, and potential applications, particularly in catalysis, and magnetic storage devices. The relationship between magnetization and NPs agglomeration has been extensively studied in previous research [46,47]. Factors such as particle size, surface charge, and synthesis conditions

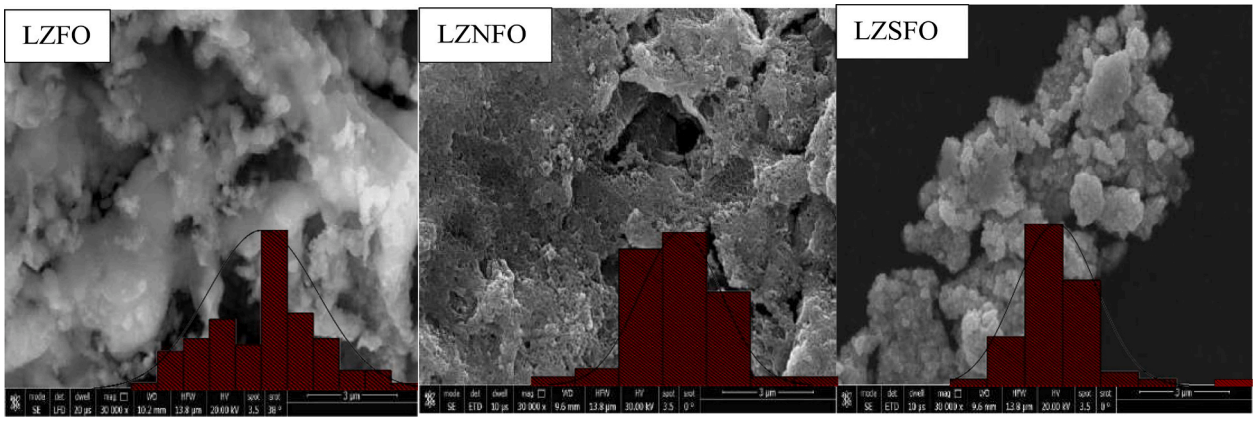

Fig. 3. FESEM micrographs of LZFO, LZNFO and LZSFO samples.

also contribute to the extent of agglomeration, affecting the material's overall properties and functionality. The histograms of grain size are illustrated in the inset of the figures. The mean grain sizes of LZFO, LZFNO, and LZFSO are 29, 27, and 24 nm, respectively. It has been noted that the mean grain size of the samples decreases with the incorporation of Nd^{3+} and Sm^{3+} into the LZFO structure. The parent SF sample exhibits a larger grain size in comparison to the REs samples, which is consistent with the XRD data.

3.1.3. Raman spectroscopy (RS)

One important technique for examining the structural disorder of materials is Raman Spectroscopy (RS). Fig. 4a–c illustrates the five Raman active modes of the SF within the range of 100–800 cm^{-1}.

The A_{1g} mode appears in the range of 600–800 cm^{-1}, corresponding to the symmetric stretching of oxygen atoms along the Fe—O or Zn—O bonds in the tetrahedral position [48].

The T_{2g} (1) modes are linked to the translational movement of the entire tetrahedron while the $T_{2g}(2)$ mode occurs in the 260–380 cm^{-1} range, attributed to the opposite motion of cation and oxygen along one direction of the lattice [47].

The symmetric and asymmetric bending modes of Li—O, Fe—O, and RE-O bonds in the B sites are associated with the E_g and $T_{2g}(3)$ modes in the region of 410–550 cm^{-1}. [49,50].

When RE^{3+} ions are introduced into LZFO, they tend to occupy the B sites because of their large ionic radii, as previously mentioned. A minor shift in the frequency of Raman bands is observed when examining various compositions (including those with and without RE^{3+}), which can provide valuable information regarding the influence of Nd^{3+}/Sm^{3+} ions on the local lattice structure. [50].

3.1.4. EDX and BET analyses

The EDX analysis of the non-stoichiometric ferrite $Li_{0.4}Zn_{0.4}RE_{0.025}Fe_{2.2}O_4$ verifies the existence of the primary constituent elements Zn, Sm, Nd, Fe, and O, whereas Li remains undetected due to its low atomic number and the inherent constraints of EDX in capturing low-energy X-rays (Fig.5). The spectrum generally displays significant peaks that correspond to the cations, indicating the successful integration of these elements into the spinel lattice. The lack of impurity peaks indicates good phase purity, while the detection of Sm^{3+}/Nd^{3+} in small concentrations confirms effective incorporating without the formation of secondary phases which agree well with XRD data. In summary, EDX offers qualitative and semi-quantitative evidence that supports the establishment of the desired LZFO, LZFNO, and LZFSO ferrite system.

BET analysis is a crucial technique for determining the surface area and porosity of materials using nitrogen gas physisorption at 77 K. The BET theory extends the Langmuir ad-sorption model by modifying it to account for multilayer ad-sorption instead of just mono layer ad-sorption [51]. As shown in Fig. 6a and b for the LZFO and LZFNO, respectively they exhibit type II isotherms which are characteristic of nonporous or microporous materials. Corresponding to the IUPAC. This type of isotherm indicates weak interactions between the nitrogen gas molecules and the sample surface, resulting in a lack of a distinct monolayer formation.

In contrast, Fig. 6c shows that the LZFSO follows a type IV isotherm, which is characterized by a mesoporous appearance of the hysteresis loop. There is a relationship between the configuration of the hysteresis loop and the texture such as pore size distribution, and pore geometry of a mesoporous sample.

IUPAC provided an empirical categorization of hysteresis loops, which was based on an earlier cataloging by de Boer [52].

The size and shape of the hysteresis loop can be qualitatively analyzed to infer details regarding the types of pores, their size distribution, and the texture of the sample. The ad-sorption hysteresis depicted in Fig. 6c (IV) is classified as type H2, which corresponds to samples that are frequently disordered, characterized.

by a distribution of pore size and shape lacking clear definition, and it also signifies the presence of bottleneck constrictions.

Furthermore, the particles possess meso- or macro-pores and

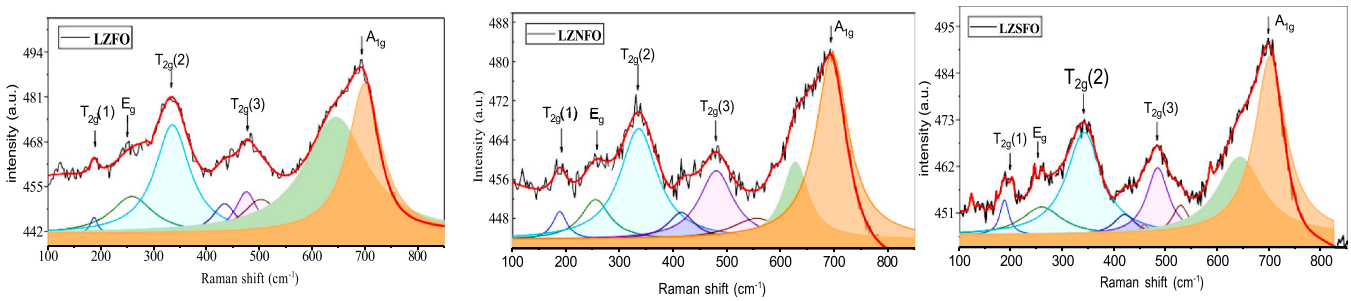

Fig. 4. a–c Raman spectra for LZFO, LZNFO and LZSFO samples.

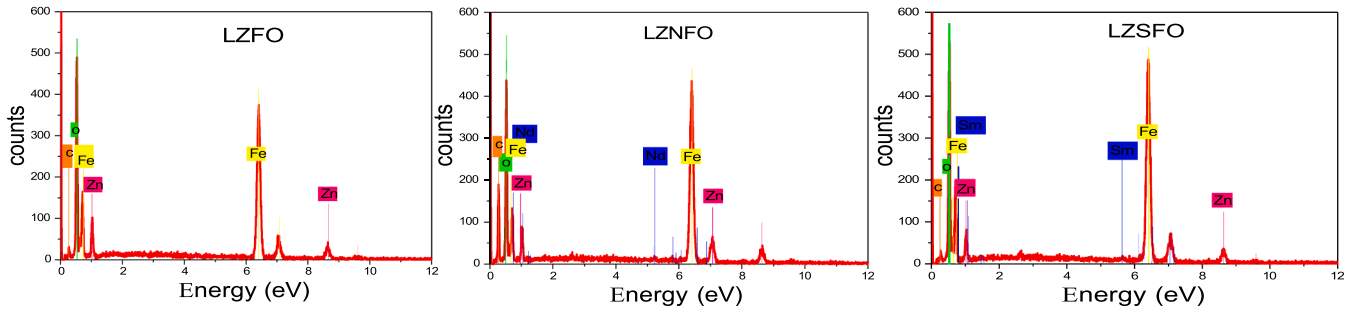

Fig. 5. EDX for LZFO, LZFNO, and LZFSO.

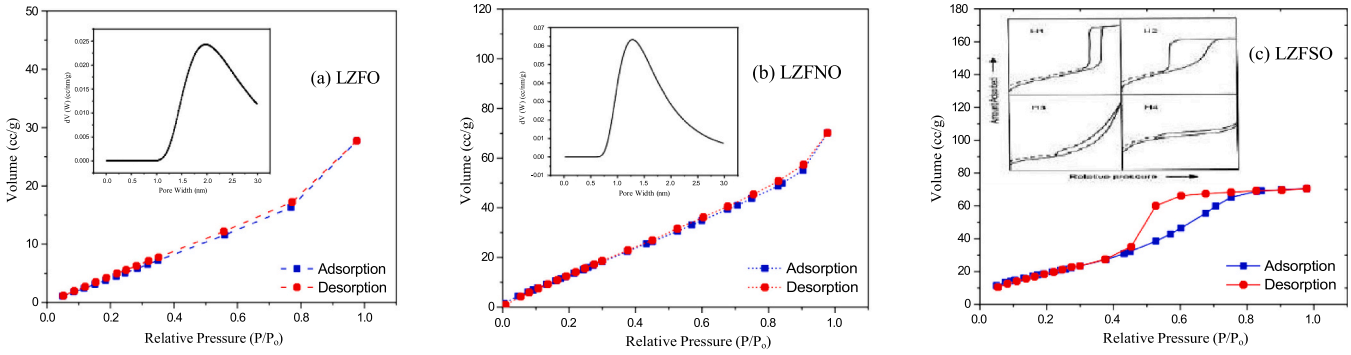

Fig. 6. a–c The adsorption/desorption isotherm of nitrogen at 77 K for all samples and distribution of pore radius.

hysteresis arises due to differences in binding constant between vapor-phase and liquid-phase nitrogen.

Theoretical surface area ($B_{Theoretical}$), can be calculated using the following Eq. [53]:

$$B_{Theoretical} = 6000/(D^{*}D_x)\left(m^2/g\right) \quad (10)$$

As observed in Table 2, the S_{BET} increases by incorporating by RE^{3+} ions, which correlates with the decrease in size as determined from XRD analysis. This reduction in D results in a higher surface -to -volume ratio, thereby exposing more surface area. Consequently, the material possesses more active surface sites, which are beneficial for various applications, including catalysis, ad-sorption, and sensor development.

3.2. Magnetic properties

3.2.1. Magnetic hysteresis (M-H) loops

The relationship between magnetization and the applied magnetic field for the LZFO, LZFSO, and LZFNO NPs is illustrated in Fig. 7. The M-H loops of the investigated samples are narrow, indicating their soft magnetic characteristics, exhibiting low coercivity (Hc) and high saturation magnetization (Ms). The combination of low coercivity and high Ms. ensures efficient magnetization and demagnetization, which is essential for applications requiring rapid magnetic response and minimal energy loss.

In SFs, the Ms. is determined by the difference between the magnetic moments on the B and A sublattices (i.e., Ms. ∝ M_B-M_A). The degree of inversion influences the distribution of cations (such as Li^{1+}, Zn^{2+}, Fe^{3+}, Fe^{2+}, or Nd^{3+}, Sm^{3+}) across these two sites. Given that the A and B sublattices are antiferromagnetically coupled, even a minor redistribution of cations can transfer magnetic ions from one sublattice to the other, thereby altering both M_A and M_B simultaneously.

Consequently, a slight modification in the inversion degree can result in a disproportionately significant change in the net moment. For instance, replacing Fe with non-magnetic cations at A sites (Zn) increases M_B- M_A, thus enhancing Ms. [54,55].

According to the Neel two-sublattice model, the theoretical values of the magnetic moment M_{AB} of a ferrimagnetic material results from the difference between the magnetization contributions of B-sites, and A-sites as described by the following Eq. [27].

$$M_{AB} = M_B - M_A \quad (11)$$

where M_B and M_A are the net magnetic moments on B and A sites, respectively [56]. On the other hand, the experimental magnetic moment (n_B) is calculated from the following equation, and the results are presented in Table 3.

The n_B is calculated using the following Eq. [57].

$$n_B = (\text{Molecular weight} \times Ms)/5585 \quad (12)$$

The discrepancy between n_B and M_{AB} as illustrated in the table can occur due to numerous factors. The first issue is deviations from the expected ideal distribution of the cations between the A-site and B-sites. The second parameter involves magnetic interaction between cations and structural defects or non-stoichiometric condition. The third factor is variations in the crystal field splitting of electronic states as illustrated in Fig. 8. Additionally, the existence of the nonlinear spin arrangement according to the Yafet–Kittel model [58].

M-H loop measurements conducted by Kokare et al. [59] demonstrated that the n_B value of Nd doped Ni—Co SFs reduced from 2.1773 μB to 0.8583 μB. The study by Amri et al. [50] revealed similar trends in n_B for $Ni_{0.6}Zn_{0.4}Al_{0.5}Nd_xFe_{1.5\text{-}x}O_4$, with the n_B value declining from 1.87 μB to 1.41 μB. The same author also detected a decline in the Ms.

Table 2
The calculated surface area (S_{BET}), pore volume, pore width and theoretical specific surface area ($B_{Theoretical}$) for the investigated samples.

Sample	S_{BET} (m^2/g)	Pore volume cc/g	Pore width (nm)	$B_{Theoretical}$ (m^2/g)
LZFO	33.42	0.043	2.57	61.9
LZFNO	61.31	0.109	3.55	69.40
LZFSO	76.61	0.109	2.86	76.30

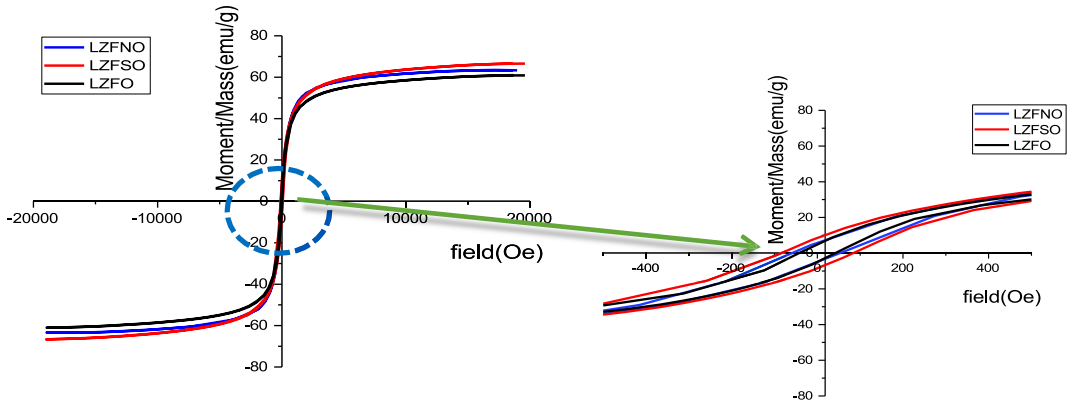

Fig. 7. Hysteresis loops of LZFO, LZFSO, and LZFNO samples.

Table 3
The estimated magnetic parameters for the investigated samples.

Sample	M_s (emu/g)	M_r (emu/g)	H_c (+Ve) (Oe)	H_c (-Ve) (Oe)	n_B	n_{th}	$M_{s\ LAS}$ (emu/g)	SFD	H_{EX} (Oe)
LZFO	61.020	4.870	41.770	−42.710	4.700	1.658	61.617	6.403	0.470
LZFNO	63.486	5.300	52.600	−59.080	4.860	1.766	63.410	8.279	3.240
LZFSO	66.628	8.480	83.960	−83.990	5.020	1.856	67.313	5.082	0.020

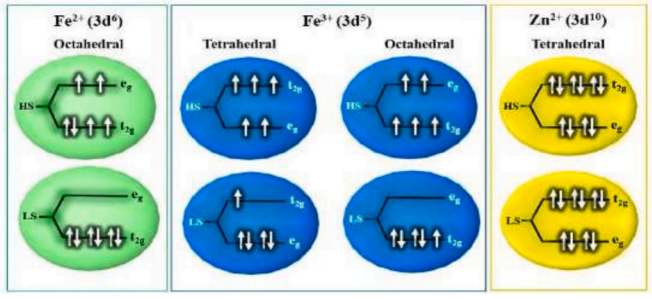

Fig. 8. The low spin and high spin configuration for A and B sites.

behavior from 47 emu/g to 34 emu/g. This decline was attributed to the doping with Nd which has a magnetic moment of 3 μB, thereby weakening the A-B super-exchange interactions and consequently lowering the M_S value. Furthermore, Hashim et al. [60] examined the Bohr magneton of Sm doped Co ferrites and noted a reduction in the n_B value from 2.65 μB to 2.16 μB. Similarly, Abdo and Daly [61] examined the fluctuations in M_S of RE doped $Co_{0.5}Cu_{0.5}Sm_xFe_{2-x}O_4$ ferrites. They observed a decline in M_S which dropped from 55.37 emu/g to 46.59 emu/g due to doping with the Sm^{3+} ions. They explained that the substitution of Sm^{3+} (1.74 μB) cations for Fe^{3+} (5 μB) ions resulted in a reduction in Ms. The same behavior has been reported by various researchers [22].

In the current study, both Nd and Sm have been observed to improve the Ms. These findings contrast with those documented by Amri et al. and Abdo et al. In our work, the incorporation of Nd^{3+} and Sm^{3+}, does not come at the expense of Fe; rather, it is an addition to it.

The magnetic behavior of the synthesized samples can be affected by their intrinsic magnetic characteristics, such as their large magnetic moment and strong spin-orbit coupling. [62]. Incorporation of RE^{3+} leads to variations in the Fe^{2+} (4 μB) /Fe^{3+} (5 μB) ratio that can greatly alter the magnetic moment by affecting electron configuration and exchange interactions. The previously mentioned parameters constitute the key issues that may impact overall magnetization. [21,55,63].

The measured values of the coercive field (H_C) are provided in Table 3. The samples exhibit small values of H_c even after the addition of RE, indicating that the spins in the magnetic domains can easily reorient under an applied external magnetic field [63]. This suggests that the addition of Sm^{3+} and Nd^{3+} does not significantly enhance magnetic anisotropy, which is typically responsible for increasing H_c. The low Hc may be attributed to a combination of factors, including the reduction in the size, as observed in Table 1, which can weaken domain wall pinning, and the maintained Fe^{3+} distribution, which preserves the soft magnetic nature of the material. Additionally, the increased surface-to-volume ratio in doped samples may contribute to enhanced surface spin disorder, further facilitating domain reorientation under an external field.

The exchange bias H_{ex}) is observed from the shift of the M-H loops from the origin, as shown in Fig. 7. This phenomenon arises due to the presence of anti-ferromagnetic (AFM) and ferro-magnetic (FM) components in the samples, likely caused by the canting of the Fe^{3+} spins. The values of H_{ex} are calculated using the following Eq. [64]:

$$H_{EX} = -[H_1 + H_2]/2 \tag{13}$$

where H_1 and H_2 signify the intercepts of the loop with the -Ve and + Ve x-axis, respectively. The presence of H_{ex} in the samples suggests their potential applicability in magnetic recording and spintronic devices, where controlled unidirectional anisotropy is desirable.

The observed shift enhances thermal stability and data retention in magnetic storage applications. Furthermore, the magnitude of H_{ex} can provide insights into the strength of exchange coupling and the extent of spin frustration at the interface, which are critical for optimizing material performance in technological applications.

The squareness ratio (SQR) [58] of the M-H loops is calculated from Eq. (14) and tabulated in the Table

$$SQR = M_r/M_s \tag{14}$$

The SQR values rise from 0.079 to 0.127 following the incorporation of Nd^{3+} and Sm^{3+} ions. This suggests that the material retains its soft magnetic nature, as having multiple domains facilitates easy magnetization reversal. Jacob et al. [65] noted that the smaller SQR values (0.08 to 0.11) signifies the anisotropic characteristics of the SF NPs. The low SQR values also imply that the H_C remains small, which aligns with the observed ease of spin reorientation under an applied field.

3.2.2. Magnetic exchange interactions (MEI)

It is known that in SFs, the Ms. depends on the EI between the A and B sites, [66]. The incorporation of Nd^{3+} and Sm^{3+} ions on B sites strongly impact the MEI among magnetic ions between the A and B sites, modifies A–B interactions, resulting in an increase in the magnitudes of Ms. and Mr. [2].

There are three credible super EIs through the oxygen anions as follows: A—A, B—B, and A–B interactions as illustrated in Fig. 9**.** These interactions depend directly on bond angle and inversely on bond length. The bond length between cations (Me–Me) (*b*, *c*, *d*, *e*, and *f*) and cation–anion (Me–O) (*p*, *q*, *r*, and *s*) are estimated using the following relations [67], which are tabulated in Table 4.

The bond angles (θ1, θ2, θ3, θ4, and θ5) between the cations and cation–anion have been calculated and tabulated in Table 5 [68].

It shows an increase in bond angles θ1, θ2, and θ5 whereas θ3 and θ4 exhibit a decrease upon the incorporation of Sm^{3+} and Nd^{3+} ions. The reduction in θ3 and θ4 suggests a weakening of B—B interactions, while the increase in θ1, θ2, and θ5 among several factors indicates a strengthening AB interaction. These results are corroborated by changes in bond length.

Although slight differences in bond angles may have a minor effect on the super exchange interaction, their extent is not adequate to account for the observed increase in Ms. The dominant contribution is more probably associated with cation distribution (alteration in inversion degree), which directly impacts the antiparallel sublattice magnetizations as previously mentioned.

3.2.3. Law of approach saturation (LAS)

To obtain a more accurate determination of the M_s, LAS is applied to the investigated NPs [69] through the following equation

$$M = M_{s\,LAS}\left(1 - A/H^2\right) \tag{15}$$

where $M_{s\,LAS}$ is the domain saturation magnetization / volume, and A is a constant controlled by the effective magneto crystalline anisotropy (k_{eff}). The relationship between magnetization M and $1/H^2$ at high external H is depicted in Fig. 10 (a–c). The intercept of the straight-line corresponds to the $M_{s\,LAS}$, which is detailed in Table 3. The values of $M_{s\,LAS}$ are found to be nearly equal to the experimental M_s derived from the loops, confirming that the applied field is sufficient to achieve saturation.

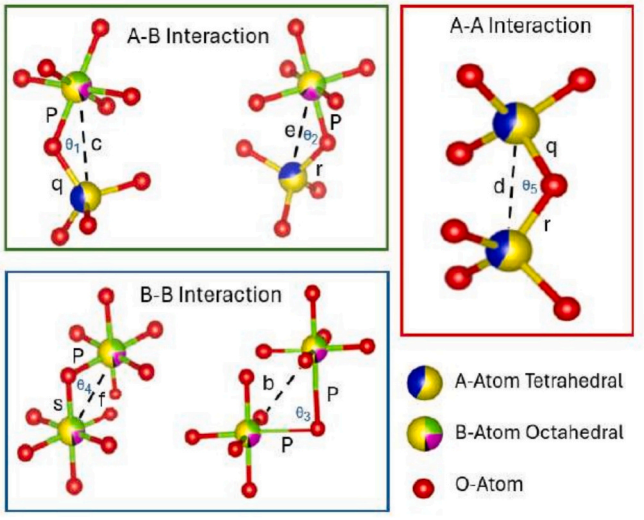

Fig. 9. Schematic arrangement of the ion pairs in In SF, exhibiting optimal lengths and angles.

3.2.4. Switching field distribution (SFD)

The rectangularity of the H-M loops and the anisotropic field are estimated using the SFD, whose value is determined using the following formula [70].

$$SFD = \Delta H/H_C \tag{16}$$

where $\Delta \boldsymbol{H}$ denotes the half width at ½ maximum (HWHM) of the dM/dH peak, which is calculated from Fig. 10(d–f).

According to A. Sebt et al. [71], a square M-H loop is accompanied with a narrow SFD, which also enhances the signal-to-noise ratio in magnetic applications. The existence of two peaks in the graph manifests the competition between exchange coupling and strong dipolar interactions within the samples [72–74]. A broader SFD implies increased inhomogeneity in local anisotropy, while a narrower SFD specifies more uniform switching behavior, which can be advantageous for sensing applications.

3.3. The removal of heavy metals (RHMs)

Although most pollutants in the waste matter can be removed by present-day water treatment facilities, the water may still contain numerous harmful ions and rapidly increasing organic contaminants. These contaminants are removed through chemi-sorption or physi-sorption on a solid surface [75–77]. Many researchers are conducting on NPS for their potential in chemical ad-sorption, attributed to their large specific surface area. Nevertheless, due to their small size, removing these ad-sorbents from the purified water can pose a considerable challenge. SFNPs are considered ideal candidates for the ad-sorption of different contaminants from water bodies [78].

The primary reason for selecting Sm^{3+} ions is their minimal size and extensive surface area, in addition to their promising magnetic properties [79,80].

3.3.1. Contact time

Fig. 11 demonstrates the impact of contact duration on the ad-sorption of Pb^{2+} ions using LZFSO ad-sorbent. The results reveal that the maximum removal efficiency (η) is achieved after 15 min of stirring, reaching approximately 90%. Subsequently, this η reduces after 60 min before increasing once more [81]. This phenomenon can be attributed to the electrostatic forces and the Van der Waals forces, which are prompted by distance. Continuous stirring likely varies the distance between the ad-sorbent surface and Pb^{2+} ions periodically, resulting in a high probability of interaction.

3.3.2. Kinetics isothermal models

For further interpretation, we will describe the kinetics isothermal models, including the pseudo first and second order, as well as the inter-particle diffusion model. The pseudo first order (PFO) equation is [82]:

$$\mathrm{Ln}(q_e - q_t) = \mathrm{Ln}\, q_e - [k_1/2.303]t \tag{17}$$

Where k_1 (min^{-1}) is the rate constant of the PFO ad-sorption, q_t denotes

the quantity of ad-sorption at time t (min) and q_e is the quantity of ad-sorption.

The PFO model is characterized by physi-sorption, which involves the absence of a chemical bond between the ad-sorbent and the ad-sorbate. This reversible process is governed by weak electro-static forces (Van der Waals bonds), where attraction adjusts with distance due to the permanent fluctuations in electron distribution that create transient dipoles.

The PSO model is portrayed by strong chemi-sorption and irreversible reactions. It depends on a chemical reaction that involves the sharing of electrons. It is represented by the following Eq. [83]:

$$t/q_t = 1/k_2 q_e^2 + t/q_e \tag{18}$$

Table 4
The calculated bond lengths for LZFO, LZFNO and LZFSO and their equations.

Me-O				Me-Me			
Equation	LZFO	LZFNO	LZFSO	Equation	LZFO	LZFNO	LZFSO
$P = a(5/8 - u)$	2.035	2.043	2.036	$b = \sqrt{2}(a/4)$	2.928	2.936	2.928
$q = a\sqrt{3}(u - 1/4)$	1.854	1.8537	1.853	$c = \sqrt{11}(a/8)$	3.433	3.442	3.434
$r = a\sqrt{11}(u - 1/4)$	3.549	3.549	3.550	$d = \sqrt{3}(a/4)$	3.586	3.595	3.587
$s = a\sqrt{3}(u/3 + 1/8)$	3.606	3.614	3.607	$e = \sqrt{3}(3a/8)$	5.379	5.393	5.379
				$f = \sqrt{6}(a/4)$	5.071	5.085	5.072

Table 5
The bond angles between M-M, and M-O.

Equation	LZFO	LZFNO	LZFSO	Equation	LZFO	LZFNO	LZFSO
$\Theta_1 = cos^{-1}(p^2 + q^2 - c^2/2pq)$	123.9	124.01	123.900	$\theta_4 = cos^{-1}(p^2 + s^2 - f^2/2ps)$	125.726	125.688	125.724
$\Theta_2 = cos^{-1}(p^2 + r^2 - e^2/2pr)$	147.51	148.05	147.540	$\theta_5 = cos^{-1}(r^2 + q^2 - d^2/2rq)$	76.020	76.310	76.050
$\theta_3 = cos^{-1}(2p^2 - b^2/2p^2)$	91.999	91.831	91.989				

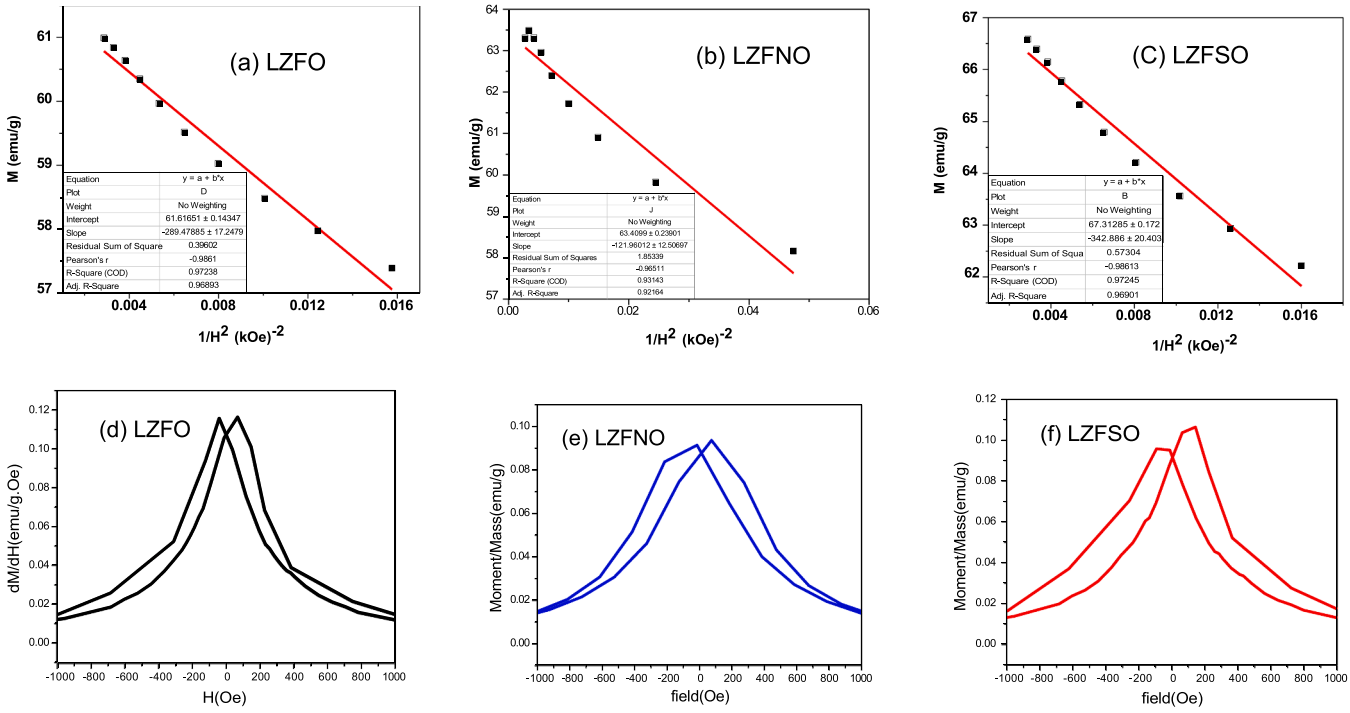

Fig. 10. (a–c) The LAS plot of the investigated samples, (d-f) The dependence of dM/dH on the magnetic field for the investigated samples.

Where k_2 [g/(mg min)]is rate constant.

Furthermore, the PSO generally takes place when there is significant interaction among ad-sorbate molecules, indicating a behavior where the interaction of the adsorbate with an already adsorbed layer is more intense than the interaction between the solid surface and the adsorbate.

The inter-particle diffusion model (IPD) defines how ad-sorbate molecules are ad-sorbed onto the active sites within the particles. The interaction is manipulated by the energetic interactions between the ad-sorbate and the ad-sorbent [84]. IPD can be represented by the following equation.

$$q_t = k_3 t^{0.5} + C \quad (19)$$

Where k_3 and C are constant. Fig. 12(a–c) illustrates the three ad-sorption kinetics models. The kinetics parameters can be deduced from the intercepts and slopes of the Figures, and the data are summarized in Table 6. The R^2 value indicates that the most dominant model in ad-sorption is the PSO [85] which is consistent with BET data.

3.3.3. Ad-sorption isotherm

The Langmuir (L.M) and Freundlich (F.M) ad-sorption isotherms for Pb^{2+} from an aqueous solution are illustrated in Fig.12d and e.

The first one assumed that the surface of ad-sorbent is homogenous and monolayer ad-sorption occurs on the surface without interactions between ad-sorbed molecules. On the other hand, F.M described the heterogeneous systems that have multilayer, so its model is most applicable in empirical experiments. The following equations represent the L. M [85]:

$$C_t/q_t = C_t/q_{max} + 1/B.q_{max} \quad (20)$$

where B is Langmuir constant related to the energy of adsorption and q_{max} is the maximum ad-sorption capacity. On the other hand, the equation of the F.M can be written as [86]:

$$log\ q_t = log\ k_f + 1/nlogC_t \quad (21)$$

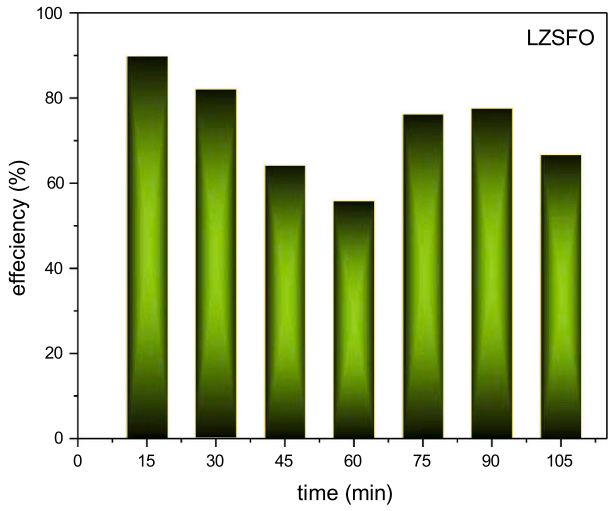

Fig. 11. The effect of contact time on the ad-sorption of Pb^{2+}ions from LZFSO adsorbent.

where k_f, is the Freundlich equilibrium constants [87], 1/n is a heterogeneous factor that indicates whether the ad-sorption process is favorable or not. Both parameters are calculated from the intercept and slope of Fig. 12e. The calculated parameters are listed in the Table.

By examining the correlation coefficients (R^2), it is evident that the experimental data align closely with both models.

Finally, one can summarize the current study in view of the interplay among structural features and magnetic characteristics of LZFO, LZFNO, and LZFSO SFs along with their efficacy as ad-sorbents in facilitating the ad-sorption of HMs from wastewater to achieve optimal removal efficiency (η). The analyzed samples present several challenges that significantly influence the ad-sorption process, as detailed in Table 1 (cation distribution + defect), Table 2 (surface area + pore size), and Table 3 (magnetization parameters).

The cation distribution, super exchange interactions, the increase in lattice parameters, reduction in particle size, and the presence of defects significantly enhance ad-sorption capacity. These factors work together to improve the performance of pollutant removal, as they are directly linked to the number of available active sites that create additional binding sites for pollutants.

The incorporation of RE^{3+} ions increases saturation magnetization and simultaneously improves lattice strain, surface area, and the number of oxygen vacancy sites. These modifications improve the binding of HM ions through mechanisms such as electrostatic attraction and ion exchange. In this way magnetic measurements can act as an indirect indicator of ad-sorption performance.

Furthermore, strong magnetic characteristics are essential for wastewater application as they facilitate the rapid and efficient separation of the ad-sorbent (LZFREO) from wastewater through the application of small external magnet. This enhances reusability and lowers operational costs.

Table 7 presents a summary of the physical properties derived from the literature survey of doped SFs, emphasizing the innovative aspects of the current study. The careful selection and concentration of RE dopants allow for the customization of SFs, thereby improving ad-sorption efficiency and expanding their range of applications. Furthermore, the comparative analysis indicates that the incorporation of Nd^{3+}/Sm^{3+} is more advantageous.

Table 6
Parameters calculated from different models.

PFO	$q_e = 0.7175$	$K_1 = 0.0714$	$R^2 = 0.801$
PSO	$q_e = 1$	$K_2 = -1.546$	$R^2 = 0.939$
IPD	$C = 0.4568$	$K_3 = 0.0725$	$R^2 = 0.361$
Langmuir	$q_{max} = 0.733$	$B = -1.024$	$R^2 = 0.979$
Freundlich	$n = -3.166$	$k_f = 1.563$	$R^2 = 0.915$

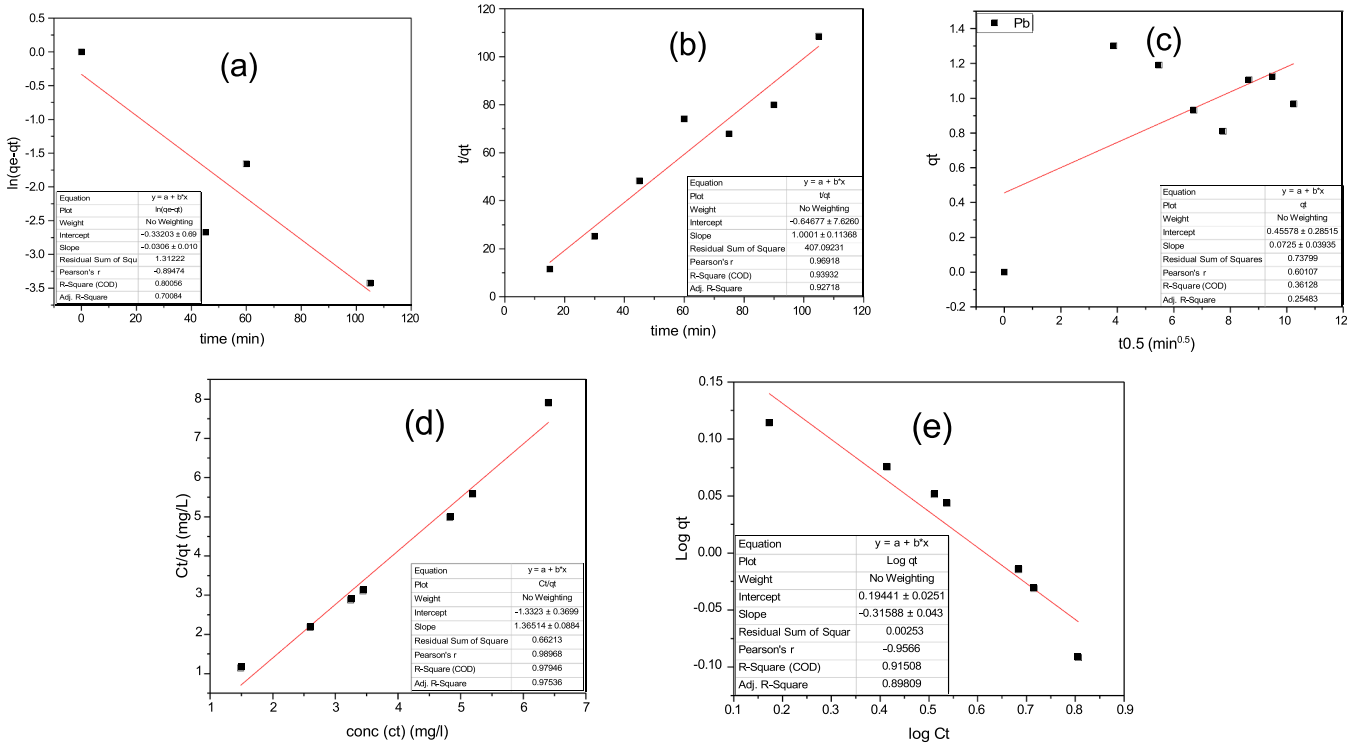

Fig. 12. Kinetics adsorption (a) PFO (b) PSO. (c) IPD (d) The Langmuir (L.) and (e) Freundlich (F.) ad-sorption isotherms models.

Table 7
A comparison of the current study and the survey.

Sample	M_S (emu/g)	M_r (emu/g)	H_C (Oe)	Size(nm)	η (%)	Ref.
$Ni_{0.1}$ $Fe_{2.9}$ O_4	37.78	–	38.29	12	73	[88]
$Cu_{0.9}Zn_{0.1}Fe_2O_4$	–	–	–	26.5–23.9	78.4	[89]
$CoFe_2$ O_4 @SiO_2 –NH_2	57	30	1379	19.04	81	[90]
$NiFe_2O_4$	49.16	–	713	30.25	79	[33]
chitosan/cobalt ferrite nanofibers	–	–	–	25	85	[91]
$Sr_{0.9}$ $Dy_{0.05}$ $Sm_{0.05}$ Fe_{12} O_{19}	53.733	26.039	3040.7	5.8820	67	[92]
$Sr_{0.95}$ $Sm_{0.05}$ Fe_{12} O_{19}	49.291	25.971	4745	5.8860	85	[92]
$Li_{0.4}Zn_{0.4}Sm_{0.025}Fe_{2.2}O_4$	66.63	8.48	83.98	15.33	90	The present work

4. Conclusion

The current research challenges the results of numerous studies that focus on the RE ions in SFs. Single-phase cubic spinel structure of non-stoichiometric $Li_{0.4}Zn_{0.4}RE_{0.025}Fe_{2.2}O_4$ nanoparticles are synthesized using the citric combustion technique. The alteration in the refined parameter u due to the incorporation of Nd^{3+} / Sm^{3+} is not merely a numerical change—it serves as direct evidence of cation redistribution, modified bond geometry, and improved magnetic behavior.

Magnetic hysteresis measurements demonstrate the soft ferrimagnetic nature of the samples. The law of approaching saturation (LAS) is applied to estimate the saturation magnetization M_S for the LZFO, LZFNO, and LZFSO samples, yielding values of 61.020, 63.486 and 66.628 emu/g, respectively.

The bond length (BL) and bond angles (θ) between cations (Me–Me) and cation–anion (Me–O) have been estimated. An increase in bond angles θ1, θ2, and θ5 is observed, whereas θ3 and θ4 exhibit a decrease upon the incorporation of Sm^{3+} and Nd^{3+} ions. The reduction in θ3 and θ4 implies a weakening of B—B interactions, while the increase in θ1, θ2, and θ5 indicates a strengthening of the AB interaction. These results are corroborated by variations in bond length.

Ultimately, the improvement in Ms. can more credibly be linked to alterations in the distribution of cations between the A and B sites, potential changes in the Fe^{2+}/Fe^{3+} ratio, and/or a decrease in spin canting effects. These elements are recognized to have a more significant impact on the overall magnetic moment in spinel ferrites and should be regarded as the main factors.

The highest adsorption capacity recorded is 90% for Pb^{2+} ions. It is concluded that the pseudo-second order model is more suitable for characterizing the ad-sorption kinetic data. The study of $Li_{0.4}Zn_{0.4}Sm_{0.025}Fe_{2.2}O_4$ spinel ferrite reveals numerous fascinating opportunities for future research, owing to its distinctive composition and possible implications. This will include investigating the effects of different Sm concentrations on the magnetic properties of the samples for use in data storage devices and magnetic sensors.

CRediT authorship contribution statement

Ebtesam E. Ateia: Writing – review & editing, Writing – original draft, Visualization, Validation, Supervision, Formal analysis, Data curation, Conceptualization. **Omnia younes:** Writing – original draft, Visualization, Validation, Methodology, Formal analysis, Data curation, Conceptualization. **M.M. Arman:** Contributed with material preparation, Data curation, Analysis, Methodology, Formal analysis, Writing and preparing the original draft, Supervision. **YA Saeid:** Contributed with material preparation, Data curation, Analysis, Methodology, Formal analysis, Writing and preparing the original draft.

Funding

No financial support.

Declaration of competing interest

The authors declare that they have no known competing financial interests or personal relationships that could have appeared to influence the work reported in this paper.

Data availability

Data will be made available on request.

References

[1] K.K. Kefeni, B.B. Mamba, T.A. Msagati, Application of spinel ferrite nanoparticles in water and wastewater treatment: a review, Sep. Purif. Technol. 188 (2017) 399–422.
[2] S. Sharma, et al., Enhancement in magnetic, dielectric properties, and specific capacitance of Mn-substituted Zn ferrite for energy storage devices, J. Mater. Sci. Mater. Electron. 36 (33) (2025) 2119.
[3] V. Ponomar, Crystal structures and magnetic properties of spinel ferrites synthesized from natural Fe–Mg–Ca carbonates, Mater. Res. Bull. 158 (2023) 112068.
[4] M. Amiri, M. Salavati-Niasari, A. Akbari, Magnetic nanocarriers: evolution of spinel ferrites for medical applications, Adv. Colloid Interf. Sci. 265 (2019) 29–44.
[5] G. Kandasamy, Recent advancements in manganite perovskites and spinel ferrite-based magnetic nanoparticles for biomedical theranostic applications, Nanotechnology 30 (50) (2019) 502001.
[6] M.F. Zawrah, H. Hamaad, S. Meky, Synthesis and characterization of nano $MgAl_2O_4$ spinel by the co-precipitated method, Ceram. Int. 33 (6) (2007) 969–978.
[7] P.A. Vinosha, et al., Synthesis and properties of spinel $ZnFe_2O_4$ nanoparticles by facile co-precipitation route, Optik 134 (2017) 99–108.
[8] J. Kwon, et al., Facile hydrothermal synthesis of cubic spinel AB_2O_4 type $MnFe_2O_4$ nanocrystallites and their electrochemical performance, Appl. Surf. Sci. 413 (2017) 83–91.
[9] C. Jiang, et al., Synthesis of spinel $LiMn_2O_4$ nanoparticles through one-step hydrothermal reaction, J. Power Sources 172 (1) (2007) 410–415.
[10] A. Noor, et al., Synthesis, morphological and electromagnetic evaluations of Ca doped Mn spinel nanoferrites for GHz regime applications, Ceram. Int. 46 (9) (2020) 13961–13968.
[11] I. Ibrahim, et al., Synthesis of magnetically recyclable spinel ferrite (MFE2O4, M= ZN, CO, MN) nanocrystals engineered by sol gel-hydrothermal technology: high catalytic performances for nitroarenes reduction, Al-Azhar Bull. Sci. 26 (1-A) (2015) 15–28.
[12] M.A. Almessiere, et al., Sonochemical synthesis and physical properties of $Co_{0.3}Ni_{0.5}Mn_{0.2}Eu_xFe_{2-x}O_4$ nano-spinel ferrites, Ultrason. Sonochem. 58 (2019) 104654.
[13] R.S. Yadav, et al., Impact of sonochemical synthesis condition on the structural and physical properties of $MnFe_2O_4$ spinel ferrite nanoparticles, Ultrason. Sonochem. 61 (2020) 104839.
[14] D.S. Mathew, R.-S. Juang, An overview of the structure and magnetism of spinel ferrite nanoparticles and their synthesis in microemulsions, Chem. Eng. J. 129 (1–3) (2007) 51–65.
[15] K. Du, H. Zhang, Preparation and performance of spinel $LiMn_2O_4$ by a citrate route with combustion, J. Alloys Compd. 352 (1–2) (2003) 250–254.
[16] A. Soufi, et al., Spinel ferrites nanoparticles: Synthesis methods and application in heterogeneous Fenton oxidation of organic pollutants–A review, Appl. Surf. Sci. Adv. 6 (2021) 100145.
[17] M.A. Maksoud, et al., La3+ doped LiCo0. 25Zn0. 25Fe2O4 spinel ferrite nanocrystals: insights on structural, optical and magnetic properties, J. Rare Earths 39 (1) (2021) 75–82.
[18] M. Ahmed, E. Ateia, S. El-Dek, Rare earth doping effect on the structural and electrical properties of Mg–Ti ferrite, Mater. Lett. 57 (26–27) (2003) 4256–4266.
[19] Z. Wang, et al., B-site Fe/Re cation-ordering control and its influence on the magnetic properties of Sr_2FeReO_6 oxide powders, Nanomaterials 12 (20) (2022) 3640.
[20] M.D. Naidu, K.B. Prakash, Rare Earth Elements in Photonic Materials, New Frontiers in Materials Science: Interdisciplinary Approaches to Innovation and Technologies (2025) 141–158.

[21] M.A. Wahba, R.K. Khaled, Sm/Gd and Sm/Gd/Nd co-doping for tailoring magnetic, dielectric, and optical properties in $CoFe_2O_4$ nanomaterials, Journal of Rare Earths (2025), https://doi.org/10.1016/j.jre.2025.11.009. Available online 7 November 2025.

[22] J. Bhemarajam, Exploring the magnetic, structural, morphological, and optical properties of Sm^{3+}-Doped Ni-Co nanoferrites and their exciting applications, 2026.

[23] W.G. Mengesha, K. Nagessar, Advanced thermal and magnetic materials for high-power and high-temperature applications: a comprehensive review, Discov. Mater. 5 (1) (2025) 180.

[24] A. Malyshev, et al., Effect of sintering regimes on the microstructure and magnetic properties of LiTiZn ferrite ceramics, Ceram. Int. 45 (2) (2019) 2719–2724.

[25] S. Mazen, N. Abu-Elsaad, Characterization and magnetic investigations of germanium-doped lithium ferrite, Ceram. Int. 40 (7) (2014) 11229–11237.

[26] V. Verma, et al., High permeability and low power loss of Ti and Zn substitution lithium ferrite in high frequency range, J. Magn. Magn. Mater. 321 (22) (2009) 3808–3812.

[27] S. Ram, S. Singh, Estimation of cation distribution in Zn0.5Mg0.5PrxFe2-xO4 ferrites using 57 Fe Mössbauer spectroscopy, Int. J. Theor. Phys. 11 (2) (2023) 88–96.

[28] N.K.C. Twarakavi, J.J. Kaluarachchi, Arsenic in the shallow ground waters of conterminous United States: Assessment, health risks, and costs for mcl compliance 1, JAWRA Journal of the American Water Resources Association 42 (2) (2006) 275–294.

[29] H. Kumari, et al., Impact of particle size on photocatalytic degradation of organic pollutants using SnO_2 nanostructures synthesized using Modified Hydrothermal method, Ceram. Int. 51 (27, Part C) (2025) 55269–55283.

[30] T. Tatarchuk, et al., Magnesium-zinc ferrites as magnetic adsorbents for Cr (VI) and Ni (II) ions removal: cation distribution and antistructure modeling, Chemosphere 270 (2021) 129414.

[31] C. Vinuthna, et al., Characterization of $Co_{1-X}Zn_xFe_2O_4$ nano spinal ferrites prepared by citrate precursor method, Int. J. Eng. Res. Appl. 3 (6) (2013) 654–660.

[32] E.E. Ateia, A.T. Mohamed, Nonstoichiometry and phase stability of Al and Cr substituted Mg ferrite nanoparticles synthesized by citrate method, J. Magn. Magn. Mater. 426 (2017) 217–224.

[33] W.A. Khoso, et al., Synthesis, characterization and heavy metal removal efficiency of nickel ferrite nanoparticles (NFN's), Sci. Rep. 11 (1) (2021) 3790.

[34] Amit V. Gongal, Deoram Nandanwar, Dilip S. Badwaik, Yograj Choudhari, Incorporating effect of rare earths (Sm^{3+} and Nd^{3+}) and transition metal ions (Al^{3+} and Cr^{3+}) in modifying the lattice structure, magnetism, and dielectric properties of magnesium copper zinc cubic ferrites, J. Magn. Magn. Mater. 622 (36) (2025) 172950, https://doi.org/10.1016/j.jmmm.2025.172950.

[35] M. Ahmed, E. Ateia, F. Salem, The effect of Ti^{4+} ions and gamma radiation on the structure and electrical properties of Mg ferrite, J. Mater. Sci. 42 (10) (2007) 3651–3660.

[36] E.E. Ateia, M.A. Ateia, M. Arman, Assessing of channel structure and magnetic properties on heavy metal ions removal from water, J. Mater. Sci. Mater. Electron. 33 (11) (2022) 8958–8969.

[37] Y. Afra, Citric acid as an organic complexing/fuel agent for the synthesis of Ce doped Co–Zn ferrite nanoparticles Yasereh Afra, Faranak Manteghi*, Mahnaz Kamel Attar Kar, Akram Omidvari Department of Chemistry, Iran University of Science and Technology, Tehran, Iran, 2014.

[38] D. Kurmude, et al., X-ray diffraction and cation distribution studies in zinc-substituted nickel ferrite nanoparticles, J. Supercond. Nov. Magn. 27 (2) (2014) 547–553.

[39] B. Venkatesh, et al., Enhanced Photocatalytic Performance of Ho^{3+} and Ce^{3+} Co-Substituted Cd-Co Spinel Ferrites by Altering the Structural, Optical, and Magnetic Properties, J. of Alloys and Compounds 1037 (2025) 182436.

[40] E.E. Ateia, et al., Multiferroic properties of $GdFe_{0.9}M_{0.1}O_3$ (M= Ag^{1+}, Co^{2+} and Cr^{3+}) nanoparticles and evaluation of their antibacterial activity, Eur. Phys. J. Plus 137 (4) (2022) 443.

[41] N. Channa, et al., Nickel-substituted manganese spinel ferrite nanoparticles for high-frequency applications, J. Mater. Sci. Mater. Electron. 31 (2020) 1661–1671.

[42] U. Holzwarth, N. Gibson, The Scherrer equation versus the'Debye-Scherrer equation', Nat. Nanotechnol. 6 (9) (2011) 534.

[43] S. Patange, et al., Cation distribution by Rietveld, spectral and magnetic studies of chromium-substituted nickel ferrites, Appl. Phys. A Mater. Sci. Process. 95 (2009) 429–434.

[44] S. Mazen, N. Abu-Elsaad, A. Nawara, Studies on micro-structure and dc conductivity of polycrystalline $Li_{0.5+0.5x}Si_xFe_{2.5-1.5x}O_4$ spinel ferrites, Powder Technol. 317 (2017) 339–347.

[45] M.M.N. Ansari, S. Khan, N. Ahmad, Influence of Dy^{3+} and Cu substitution on the structural, electrical and dielectric properties of $CoFe_2O_4$ nanoferrites, J. Mater. Sci. Mater. Electron. 30 (19) (2019) 17630–17642.

[46] A.L. Vadivelu, et al., Synthesis and characterisation of MFe2O4 (M= Zn, Cu) spinel ferrite nano particles, J. Pharm. Negat. Results (2022) 7650–7656.

[47] Z. Ahmad, et al., Surface morphological characterization of Co1-xCexFe2O4 spinel ferrites synthesized by solid state reaction method, Adv. Nanopart. 12 (3) (2023) 139–146.

[48] P. Galinetto, et al., Raman spectroscopy in zinc ferrites nanoparticles, Raman Spectrosc 223 (2018) 228.

[49] T.S. Almutairi, Unveiling the impact of spin and cation dynamics on Raman spectroscopy in Co-Ferrite, ACS Phys. Chem. 5 (2025) 171–182.

[50] B.D. Hosterman, Raman spectroscopic study of solid solution spinel oxides, 2011.

[51] S.B. Somvanshi, et al., Hydrophobic to hydrophilic surface transformation of nano-scale zinc ferrite via oleic acid coating: magnetic hyperthermia study towards biomedical applications, Ceram. Int. 46 (6) (2020) 7642–7653.

[52] M. Donohue, G. Aranovich, Adsorption hysteresis in porous solids, J. Colloid Interface Sci. 205 (1) (1998) 121–130.

[53] S.B. Somvanshi, et al., Structural, thermal, spectral, optical and surface analysis of rare earth metal ion (Gd^{3+}) doped mixed Zn–Mg nano-spinel ferrites, Ceram. Int. 46 (9) (2020) 13170–13179.

[54] Jinpei Lin, Xingxing Yang, Kaimin Su, Fang Yang, Yun He, Qing Lin, Effects of nonmagnetic Zn2+ ion and RE ion substitution on the magnetic properties of functional nanomaterials Co1−yZnyRExFe2−xO4 (RE=La,Sm,Gd) by Sol–Gel, Molecules 28 (17) (2023) 6280, https://doi.org/10.3390/molecules28176280.

[55] Karla R. Sanchez-Lievanos, James L. Stair, Kathryn E. Knowles, Cation distribution in spinel ferrite nanocrystals: characterization, impact on their physical properties, and opportunities for synthetic control, Inorg. Chem. 60 (7) (2021).

[56] E.E. Ateia, et al., Effect of different Gd^{3+} ion content on the electric and magnetic properties of lithium antimony ferrite, J. Inorg. Organomet. Polym. Mater. 26 (1) (2016) 81–90.

[57] E.E. Ateia, et al., The impact of Ni substitution on the structural and magnetic properties of Mg nano-ferrite, Silicon 10 (4) (2018) 1687–1696.

[58] N. Kolmakova, et al., Field-induced magnetic phase transitions in the Yafet-Kittel model, Phys. Solid State 41 (10) (1999) 1649–1651.

[59] M. Kokare, et al., Effect of Nd^{3+} doping on structural and magnetic properties of $Ni_{0.5}Co_{0.5}Fe_2O_4$ nanocrystalline ferrites synthesized by sol-gel auto combustion method, J. Alloys Compd. 748 (2018) 1053–1061.

[60] M. Hashim, et al., Influence of samarium doping on structural, elastic, magnetic, dielectric, and electrical properties of nanocrystalline cobalt ferrite, Appl. Phys. A Mater. Sci. Process. 127 (7) (2021) 526.

[61] M. Abdo, A. El-Daly, Sm-substituted copper-cobalt ferrite nanoparticles: preparation and assessment of structural, magnetic and photocatalytic properties for wastewater treatment applications, J. Alloys Compd. 883 (2021) 160796.

[62] A. Ait Taleb, et al., Ferromagnetism and magnetic anisotropy induced in rare-earth (La, Ce, Pr, Nd, Pm, and Sm)-doping 2D Sn monolayers, J. Supercond. Nov. Magn. 38 (1) (2025) 36.

[63] M.A. Almessiere, et al., Effects of Ce–Dy rare earths co-doping on various features of Ni–Co spinel ferrite microspheres prepared via hydrothermal approach, J. Mater. Res. Technol. 14 (2021) 2534–2553.

[64] R.M. Khafagy, E. El-Khawas, Controlling the magnetic characters co-existing at the novel nanometric multiferroic $PrAl_xFe_{1-x}O_3$; $0.0 \leqslant x \leqslant 0.6$ via an exchange bias interaction to open a new era of applications, J. Alloys Compd. 606 (2014) 288–297.

[65] B.P. Jacob, et al., Effect of Tb^{3+} substitution on structural, electrical and magnetic properties of sol–gel synthesized nanocrystalline nickel ferrite, J. Alloys Compd. 578 (2013) 314–319.

[66] K. Pal, S. Mandal, I. Das, The investigation of the influence of B-site disorder on giant exchange bias: experimental observations and theoretical insights, Acta Mater. 278 (2024) 120276.

[67] E.E. Ateia, K. Meleka, F. Ghobrial, Interplay between cation distribution and magnetic properties for $CoAl_xFe_{2-x}O_4$ $0.0 \leq x \leq 0.7$ nanoparticles, Appl. Phys. A Mater. Sci. Process. 127 (11) (2021) 831.

[68] L. Phor, S. Chahal, V. Kumar, Zn^{2+} substituted superparamagnetic $MgFe_2O_4$ spinel-ferrites: Investigations on structural and spin-interactions, J. Adv. Ceram. 9 (5) (2020) 576–587.

[69] K. Raju, G. Venkataiah, D. Yoon, Effect of Zn substitution on the structural and magnetic properties of Ni–Co ferrites, Ceram. Int. 40 (7) (2014) 9337–9344.

[70] E.E. Ateia, Abdulalah AL-Hamzi, Fatma M. Ahmed, Amira T. Mohamed, Synthesis and characterization of high entropy oxides for supercapacitor applications, Under publication in energy storage, 2026.

[71] A. Sebt, M. Akhavan, Switching field distribution of magnetic fine particles, J. Magn. Magn. Mater. 237 (1) (2001) 111–118.

[72] E.E. Ateia, K. Elsayed, D. El-Nashar, Tuning the properties of NBR/$BaFe_{11.5}Co_{0.5}O_{19}$: a road toward diverse applications, Appl. Phys. A Mater. Sci. Process. 129 (2) (2023) 118.

[73] D. Han, et al., Influence of size and magnetocrystalline anisotropy on spin canting anomaly in fine ferrimagnetic particles, J. Appl. Phys. 76 (10) (1994) 6591–6593.

[74] M. Arman, The influence of rare earth doping on the structure, magnetic properties, and application of $LaFeO_3$ nanoparticles, The European Physical Journal Plus 140 (3) (2025) 1–10.

[75] H. Kumari, et al., Hydrothermally synthesized $ZnFe_2O_4$/ZnO heterojunction nanocomposites for enhanced RB dye degradation via Z-scheme photocatalysis, Mater. Chem. Phys. 322 (2024) 129560.

[76] A. Kumar, MoS_2/ZnO nanocomposites for efficient degradation of organic dyes and real industrial wastewater via photocatalytic process, Mater. Sci. Eng. B 329 (2026) 119400.

[77] A. Kumar, Designing MoS_2/CeO_2 heterostructures via one-pot ultrasonication for MB dye degradation, Ceram. Int. 51 (24, Part B) (2025) 43070–43083.

[78] D. Kerkez, et al., Metal nanoparticles in dye wastewater treatment–smart solution for clear water, Recent Pat. Nanotechnol. 15 (3) (2021) 270–294.

[79] M. Irfan, et al., Statistically analyzed heavy metal removal efficiency of silica-coated $Cu_{0.50}Mg_{0.50}Fe_2O_4$ magnetic adsorbent for wastewater treatment, ACS Omega 8 (50) (2023) 47623–47634.

[80] L. Guo, et al., Effect of Sm^{3+} ions doping on structure and magnetic properties of nanocrystalline $NiFe_2O_4$ fibers, J. Alloys Compd. 490 (1–2) (2010) 301–306.

[81] P. Punia, et al., Adsorption of Cd and Cr ions from industrial wastewtater using Ca doped Ni–Zn nanoferrites: synthesis, characterization and isotherm analysis, Ceram. Int. 48 (13) (2022) 18048–18056.

[82] E.E. Ateia, Yousra Yasser, Amira S. Shafaa, Fabrication, characterization and adsorption of lead ions by doped barium hexaferrite nanoparticles, J. Sol-Gel Sci. Technol. 117 (2026) 50.

[83] D. Robati, Pseudo-second-order kinetic equations for modeling adsorption systems for removal of lead ions using multi-walled carbon nanotube, J. Nanostructure Chem. 3 (1) (2013) 55.
[84] F.-C. Wu, R.-L. Tseng, R.-S. Juang, Initial behavior of intraparticle diffusion model used in the description of adsorption kinetics, Chem. Eng. J. 153 (1–3) (2009) 1–8.
[85] M. Khosravani, et al., Efficient lead removal from aqueous solutions using a new sulfonated covalent organic framework: Synthesis, characterization, and adsorption performance, Arab. J. Chem. 17 (1) (2024) 105429.
[86] C.-h. Yang, Statistical mechanical study on the Freundlich isotherm equation, J. Colloid Interface Sci. 208 (2) (1998) 379–387.
[87] M. Firdaus, et al., Derivation and constants determination of the Freundlich and (fractal) Langmuir adsorption isotherms from kinetics, in: IOP Conference Series: Materials Science and Engineering, IOP Publishing, 2018.
[88] E.E. Ateia, Samah Fouad, Amira T. Mohamed, Characterization of spinel ferrite nano composites: from synthesis to applications, Appl. Phys. A Mater. Sci. Process. 131 (2025) 980.
[89] G.M. Jaid, A.J. Bohan, G.K. Salman, Artificial neural network modeling for removal of Cd (II) and Pb (II) from wastewater by using three ferrite nanomaterials ($Cu_{0.9}Zn_{0.1}Fe_2O_4$, $Cu_{0.8}Zn_{0.2}Fe_2O_4$, and $Cu_{0.7}Zn_{0.3}Fe_2O_4$) and study the antimicrobial effectiveness of these ferrite substances, Rev. Chim. 71 (10) (2020) 67–80.
[90] M.U. Saleem, et al., Study of kinetics and the working mechanism of silica-coated amino-functionalized $CoFe_2O_4$ ferrite nanoparticles to treat wastewater for heavy metals, ACS Omega 9 (3) (2024) 3507–3524.
[91] M. Aliabadi, Removal of Pb (II) and Cr (VI) ions from aqueous solutions using chitosan/cobalt ferrite nanofibrous adsorbent, Fibers Polym. 17 (8) (2016) 1162–1170.
[92] E.E. Ateia, Salma Aboelnasr, Amira T. Mohamed, Magneto-fluorescent $ZnFe_2O_4$/CQDs nanoparticles derived from lemon peels for biomedical applications, Diam. Relat. Mater. 164 (2026) 113477.